

MaskBlur: Spatial and Angular Data Augmentation for Light Field Image Super-Resolution

Wentao Chao, Fuqing Duan, Yulan Guo, *Senior Member, IEEE*, Guanghui Wang, *Senior Member, IEEE*

Abstract—Data augmentation (DA) is an effective approach for enhancing model performance with limited data, such as light field (LF) image super-resolution (SR). LF images inherently possess rich spatial and angular information. Nonetheless, there is a scarcity of DA methodologies explicitly tailored for LF images, and existing works tend to concentrate solely on either the spatial or angular domain. This paper proposes a novel spatial and angular DA strategy named MaskBlur for LF image SR by concurrently addressing spatial and angular aspects. MaskBlur consists of spatial blur and angular dropout two components. Spatial blur is governed by a spatial mask, which controls where pixels are blurred, i.e., pasting pixels between the low-resolution and high-resolution domains. The angular mask is responsible for angular dropout, i.e., selecting which views to perform the spatial blur operation. By doing so, MaskBlur enables the model to treat pixels differently in the spatial and angular domains when super-resolving LF images rather than blindly treating all pixels equally. Extensive experiments demonstrate the efficacy of MaskBlur in significantly enhancing the performance of existing SR methods. We further extend MaskBlur to other LF image tasks such as denoising, deblurring, low-light enhancement, and real-world SR. Code is publicly available at <https://github.com/chaowentao/MaskBlur>.

Index Terms—Light field, data augmentation, super-resolution.

I. INTRODUCTION

LIGHT Field (LF) [1]–[5] images capture spatial and angular information of a scene in a single shot using an LF camera, giving rise to various important applications such as refocusing, depth estimation [6]–[8], view synthesis [9], and 3D reconstruction [10]. However, due to the inherent limitations of commercialized LF cameras, there is a trade-off between spatial and angular resolution in LF images. To enhance the spatial resolution of LF images, traditional methods typically rely on the geometric information of the LF and manually designed features for super-resolution (SR), which have limited performance and slow processing speed. In recent years, deep learning-based LF image SR methods [11]–[18] have made significant progress in terms of accuracy and

W. Chao and F. Duan are with the School of Artificial Intelligence, Beijing Normal University, Beijing 100875, China. (e-mail: chaowentao@mail.bnu.edu.cn; fqduan@bnu.edu.cn).

Y. Guo is with the School of Electronics and Communication Engineering, Sun Yat-sen University, Guangzhou 510275, China. (e-mail: guoyulan@syzu.edu.cn)

G. Wang is with the Department of Computer Science, Toronto Metropolitan University, Toronto, ON M5B 2K3, Canada. (e-mail: wangcs@torontomu.ca).

This work is supported by the National Key Research and Development Project Grant, Grant/Award Number: 2018AAA0100802.

Manuscript received May 31, 2024; revised August 13, 2024; accepted September 06, 2024. Corresponding author: F. Duan

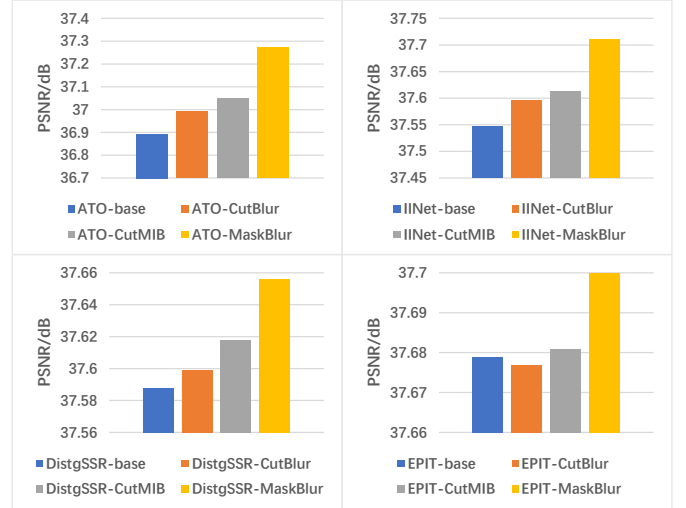


Fig. 1. Comparison MaskBlur with CutBlur [19] and CutMIB [20] on various LF image SR methods, i.e., ATO [21], IINet [2], DistgSSR [12] and EPIT [22]. We compare the average PSNR (dB, \uparrow) on the HCIold [23] dataset. Note that MaskBlur improves the values of PSNR by a large margin compared to other DA schemes on various LF image SR methods.

speed. Nevertheless, the performance of these methods is still constrained by the available dataset size, and collecting a large-scale LF dataset is time-consuming and labor-intensive. Therefore, exploring efficient data augmentation (DA) techniques specifically for LF images SR is highly desirable.

Many previous methods on DA primarily focus on high-level vision tasks such as image classification [24] and object detection [25]. However, few studies have been performed on DA specifically for LF image SR. The commonly used DA techniques for LF image SR tasks still mainly rely on geometric transformations, e.g., horizontal and vertical flips. A recent study in [19] demonstrated the importance of maintaining spatial structure consistency for image SR, i.e., low-resolution (LR) and high-resolution (HR) have the same structure and further introduced the CutBlur DA strategy by randomly exchanging pixels between LR and the corresponding HR regions through a *cutting-pasting* operation. While a direct extension of CutBlur from general images to LF images is a straightforward approach, i.e., applying CutBlur to each LF sub-aperture image (SAI), as shown in Fig. 2 (a). However, this approach only maintains spatial structure consistency of the LF image while neglecting to augment the angular domain, and the latter has been validated to be crucial for LF image SR works [12], [21]. A subsequent study [20] proposed CutMIB that implicitly utilizes the angular (multi-

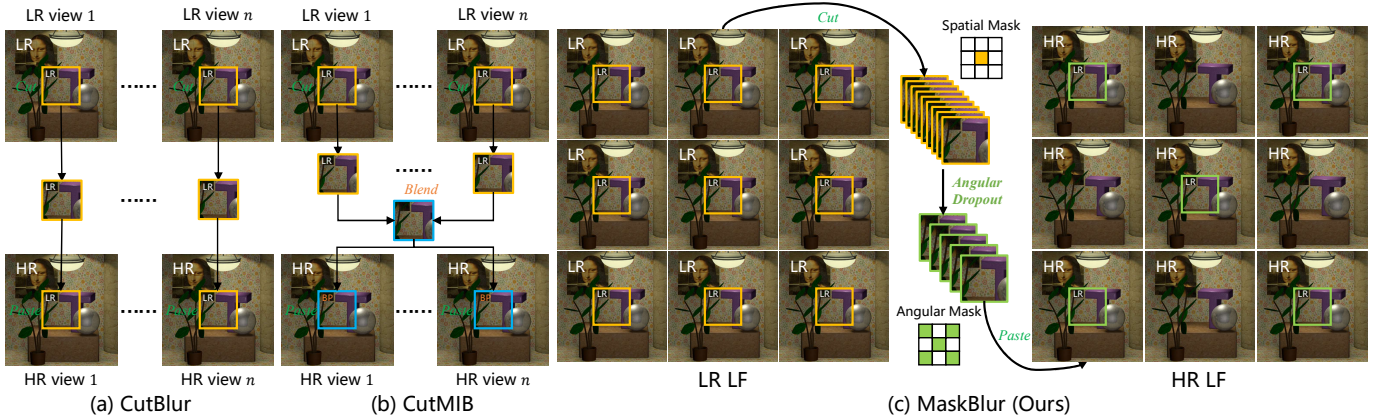


Fig. 2. Detailed comparisons of MaskBlur with CutBlur [19] and CutMIB [20]. MaskBlur consists of spatial blur and angular dropout, which are implemented through the spatial and angular masks, respectively.

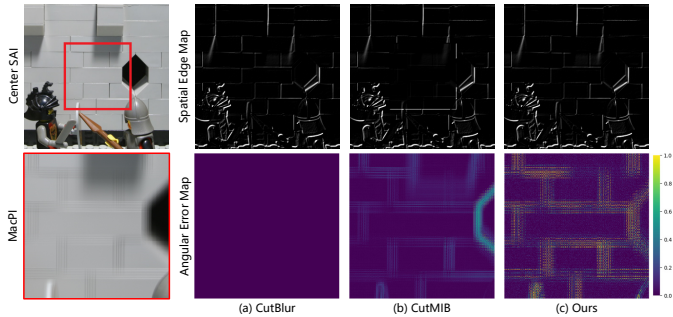


Fig. 3. Analyzing CutBlur [19], CutMIB [20] and MaskBlur from spatial and angular domain. The center SAI is in a 5×5 LF. The red rectangle denotes the area for the cutting and pasting operation, i.e., cut an LR patch and paste it to the original HR image. Macro-pixel image (MacPI) represents the pasted region in the angular domain. The spatial edge map is generated by using *Sobel* operation on the augmented HR LF image the angular error map is calculated between LR and augmented HR LF in the angular domain. MaskBlur can maintain spatial structure consistency and enhance angular domain information. Please zoom in for better visualization.

view) information of the LF image by involving a *cutting-blending-pasting* operation, e.g., cropping patches of each LR SAI, blending them, i.e., calculate the mean of these patches, and pasting the blended patch onto corresponding HR SAIs, as shown in Fig. 2 (b). However, CutMIB implicitly enhances the angular information of the LF image, it does not consider the differences between individual SAIs and disrupts spatial structure consistency, thereby limiting its performance.

To better demonstrate our observations, we provide visual comparisons using the spatial edge map, which contains structure information, and the angular error map to represent angular domain information difference in Fig. 3. Specifically, we use CutBlur or CutMIB on the LR center view in a 5×5 LF, cut an LR patch or cut and blend an LR patch, and then paste it to the original HR image. Finally, we adopt *Sobel* operation on augmented HR LF image to generate the spatial edge map and calculate the angular error map between LR and augmented HR LF in the angular domain. We can directly observe from the spatial edge map in Fig. 3(a) that the CutBlur strategy has the complete edge in the pasted patch region which can represent it maintains spatial structure consistency,

but it does not augment the information of angular domain, i.e., the information of pasted region all comes from LR domain (see angular error map in Fig. 3(a)). Then, we can see from the angular error map in Fig. 3(b) that the CutMIB strategy provides additional angular (multi-view) information in the pasted region. However, the spatial edge map in Fig. 3(b) shows that the CutMIB has obvious edge differences adjacent to the pasted region, and the original edge information is missing inside the region i.e., it cannot maintain spatial structure consistency.

To simultaneously augment both spatial domain and angular domain information based on the observations above, this paper proposes a novel DA approach called MaskBlur for LF image SR (see Fig. 2 (c)). The spatial edge map and angular error map in Fig. 3 (c) shows that our method not only preserves structure consistency in the spatial domain (i.e., maintaining the same edge structure) but also incorporates angular domain information from distinct LR and HR spaces. Specifically, MaskBlur comprises spatial blur and angular dropout, which are responsible for enhancing spatial and angular information, respectively. Firstly, spatial blur determines which regions of the LR and HR images need pixel swapping by randomly generating a spatial mask. Secondly, angular dropout selects which views are subjected to spatial blur operations based on a randomly generated angular mask. MaskBlur enables the LF image SR model to treat pixels in the spatial and angular domains differently, thus improving model regularization. Fig. 1 illustrates that MaskBlur improves the values of PSNR by a large margin compared to other DA schemes on various LF image SR methods while maintaining the network structures unchanged. Moreover, we verify the effectiveness of the MaskBlur on real-world LF image SR, denoising, and deblurring tasks.

In summary, the contributions of this paper are as follows:

- This paper proposes MaskBlur, a simple yet effective DA scheme for LF image SR. MaskBlur is designed to preserve spatial structure consistency while simultaneously enhancing angular domain information.
- MaskBlur comprises spatial blur and angular dropout two key components. Spatial blur determines which regions

of the LR and HR images need pixel swapping by randomly generating a spatial mask. Angular dropout selects which views undergo spatial blur operations based on a randomly generated angular mask.

- The efficacy of MaskBlur is substantiated through comprehensive experiments across diverse LF image SR methods. Moreover, MaskBlur can be extended to other LF image processing tasks, such as LF image denoising, deblurring, and real-world SR.

II. RELATED WORK

This section briefly reviews the related works of the LF image SR task and the DA in computer vision.

A. LF image SR.

LF image SR aims to generate HR LF images from LR LF inputs. One straightforward approach for LF image SR is to independently apply single-image super-resolution (SISR) methods to each SAI. However, directly applying SISR methods to LF images may not produce satisfactory results as it overlooks the correlations between different viewpoints. To achieve high-performance LF image SR, it is important to fully exploit the information within a single viewpoint (i.e., spatial information) and across different viewpoints (i.e., angular information).

Traditional Methods. Traditional methods for LF image SR relied on the geometric structure [26] and mathematical modeling [27] of the LF, which utilized projection and optimization techniques to super-resolve LR images. Bishop *et al.* [28] first restores the scene depth, and then uses the Bayesian deconvolution method to obtain HR results. Mitra *et al.* [29] introduced a Gaussian mixture model to encode the structure of the LF for LF image SR. Wanner *et al.* [27] utilized the structure tensor to deduce depth from Epipolar Plane Images (EPIs), employing this data to refine the resolution of view images through interpolation. Farrugia *et al.* [30] decomposed HR and LR image patches into subspaces and proposed a linear subspace projection method. Alain *et al.* [31] extended the BM3D [32] filter to LFBM5D for LF denoising and spatial SR. Rossi *et al.* [33] developed a graph-based approach to achieve spatial super-resolution through graph optimization. However, these methods are computationally intensive and have lower accuracy.

Deep learning-based Methods. In recent years, CNN-based [34] and Transformer-based methods [11], [22], [35] have become mainstream, demonstrating significant improvements in speed and accuracy compared to traditional approaches. LFCNN [34] was the first CNN-based method that learns the correspondence between the LF stacked sub-aperture images (SAIs). Jin *et al.* [21] proposed LFSSR-ATO, a *all-to-one* LF image SR method, which incorporates structural consistency regularization to preserve disparity structures. Wang *et al.* [36] proposed an LF-InterNet interact spatial and angular information for LF image SR. Zhang *et al.* [37] divided the LF into four different branches based on specific angular directions and utilized four sub-networks to model the spatial-angular correlations. Liu *et al.* [2] proposed LF-IINet to

exploit the correlations among all views and simultaneously preserve the parallax structure of LF views. Wang *et al.* [12] disentangled the spatial-angular correlation and proposed the method DistgSSR for LF image SR. Liang *et al.* [11] applied the Transformer to LF image SR for the first time and designed a Spatial Transformer and Angular Transformer to incorporate spatial and angular information respectively. Wang *et al.* [35] treated LF image SR as a sequence-to-sequence reconstruction task and designed a DPT to leverage gradient maps of LF to guide the sequence learning. While existing methods concentrate on optimizing the utilization of spatial and angular information in LF images, their performances frequently face limitations stemming from the size of the LF dataset. More recently, EPIT [22] has delved further into addressing the challenges posed by large disparity variations inherent in LF. HLFSR [15] proposed an inter-intra spatial feature extractor and an inter-intra angular feature extractor to leverage the correlations among pixels in the spatial-angular domain. LF-DET [5] introduced a deep efficient transformer architecture with a spatial-angular separable transformer encoder. It incorporates sub-sample spatial modeling and multi-scale angular modeling to facilitate global context interaction.

We focus on an orthogonal direction, i.e., the perspective of DA. The proposed approach, MaskBlur, offers generalization and can be applied to different LF image SR methods effectively.

B. DA in Computer Vision

DA in high-level vision. DA techniques have been widely studied for high-level vision tasks, such as image classification [25]. These techniques are primarily implemented in pixel space and feature space. In pixel space, general DA strategies include geometric and color transformations, i.e., translation, rotation, flipping (horizontal or vertical), color jitter, RGB permute, and blending. Mixup [38] randomly selected two images and blended them in proportion to generate unseen training samples. Cutout [39] randomly removed selected regions in an image. CutMix [40] combined the advantages of Mixup and Cutout by replacing randomly removed regions with content from another image. Hide-and-seek [41] divided an image into grids and randomly hid image blocks for model training. AutoAugment [42] focused on automatically learning the optimal augmentation strategy. Recently, BEiT [43] and MAE [44] have used the random masking strategy to restore the masked tokens or pixels in a self-supervised manner for pre-training image transformers. In feature space, some methods are specifically designed to enhance the features of CNNs, including feature mixing, shaking, and dropping. Feature mixing is similar to Mixup, while Manifold Mixup [45] blended the features of two images in feature space. Shake-shake introduced multiple branches in the network and performed random shaking operations in each branch. Shake-Shake [46] and ShakeDrop [47] introduced random pruning operations. DropPath [48] randomly drooped certain connections in the network during training. However, these methods are primarily designed for high-level vision tasks and may lose spatial structure information, which is important for low-level vision tasks, such as SR and denoising.

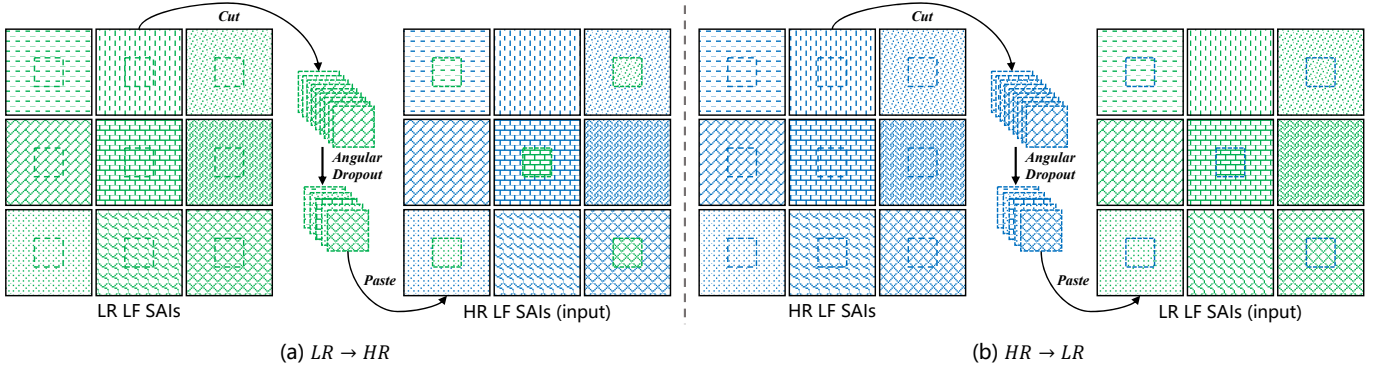


Fig. 4. Semantic illustration of MaskBlur. Here, an LF of size $U = V = 3, H = W = 3$ is used as a toy example. LR LF SAIs and HR LF SAIs are painted with green and blue background color. Different textures denote different views. We show the examples of $LR \rightarrow HR$ and $HR \rightarrow LR$. Better to view in color and texture.

DA in low-level vision. [49] proposed seven techniques to improve the performance of single-image SR, including pixel geometric transformations such as horizontal flipping, vertical flipping, and rotation. [50] analyzes the application of Mixup in single-image SR to mitigate model overfitting. CutBlur [19] comprehensively analyzed existing DA methods for SR tasks, highlighted the importance of maintaining spatial structure consistency, and proposed the *cutting-pasting* operation to exchange information between LR and HR images to generate new training samples. However, the CutBlur method mainly operates in the spatial domain and does not consider the angular information when LF image SR. Recently, [20] introduced a DA strategy CutMIB for LF image SR task which leverages multi-view information during the training phase. CutMIB involves a *cutting-blending-pasting* operation, i.e., cropping and blending random regions of each LR SAI and pasting them onto corresponding HR SAIs. However, while CutMIB implicitly utilizes the multi-view information of LF images, it does not consider the differences between individual SAIs and may disrupt spatial structure consistency.

In this study, we propose MaskBlur, a DA strategy designed to enhance spatial and angular information through spatial blur and angular dropout. Our approach not only preserves spatial structure consistency but also effectively enhances the angular information of LF images.

III. METHOD

A. Preliminary

We adopt the two-plane LF parameterization model [51] to represent an LF image, which can be formulated as a 4D function $\mathcal{L}(u, v, h, w) \in \mathbb{R}^{U \times V \times H \times W}$, where U and V stand for angular dimensions, H and W denote spatial dimensions. LF image SR networks aim to learn the mapping function $f_\theta(\cdot)$ and take an LR LF $\mathcal{L}_{LR} \in \mathbb{R}^{U \times V \times H \times W}$ as input and generate the SR LF $\mathcal{L}_{SR} \in \mathbb{R}^{U \times V \times \alpha H \times \alpha W}$ as output, where α stands for the scale factor of SR, which can be denoted as $\mathcal{L}_{SR} = f_\theta(\mathcal{L}_{LR})$, where θ is the parameters of the LF image SR network. The reconstructed SR LF is desired to be close to the ground-truth HR LF $\mathcal{L}_{HR} \in \mathbb{R}^{U \times V \times \alpha H \times \alpha W}$. The LF image SR network is optimized with a loss function, and L_1 is the most commonly used one. Given a training set $\mathcal{L}_i^{LR}, \mathcal{L}_i^{HR}$,

which contains N LR input LF and HR counterpart. The goal of training the LF image SR network is to minimize the L_1 loss function:

$$L = \frac{1}{N} \sum_{i=1}^N \|f_\theta(\mathcal{L}_i^{LR}) - \mathcal{L}_i^{HR}\|_1 \quad (1)$$

In our experiments, we set $\alpha = 4$ to evaluate the impact of DA on various models' performance. Most mainstream LFSR methods opt for a scaling factor of $\alpha = 4$ for $4\times$ super-resolution tasks. This choice provides a reliable baseline model and facilitates the comparison of different DA schemes against the baseline. Additionally, the $4\times$ super-resolution task is more challenging than the $2\times$, better reflecting the impact of DA schemes. Therefore, we ultimately chose $\alpha = 4$ for $4\times$ super-resolution tasks.

B. Motivation

Currently, common DA techniques used in LF image SR tasks mainly involve geometric transformations, such as horizontal or vertical flips. However, these geometric transformations do not consider the characteristics of the SR task, where images may contain varying degrees of blurriness that need to be treated differently by the model. Therefore, the effectiveness is limited. CutBlur [19] was specifically designed for the single SR task and could maintain the spatial structure consistency of the augmented image through the *cutting-pasting* operation. However, extending CutBlur directly from single images to LF images does not enhance the angular domain information, i.e., all the information comes from the LR or HR image when extracting the angular domain features. Subsequent work, CutMIB [20], utilized multi-view information and implicitly enhances the angular domain (multi-view) information through *cutting-blending-pasting* operations. However, all the pasted regions from different viewpoints contain the same spatial information, which violates the spatial structure consistency. LF images consist of both spatial and angular information. Therefore, we think that a better DA technique is needed to augment simultaneously LF images in both spatial and angular domains. Specifically, we extend the CutBlur operation to spatial blur in the spatial domain. We control the

position of the pasted region using a patch-based random spatial mask instead of a rectangle mask. In the angular domain, drawing inspiration from the commonly used regularization technique Dropout [52], we introduce an additional operation called Angular Dropout. By using a random angular mask, we perform random selections on the viewpoints to control whether the spatial blur operation is applied. The pasted region in the angular domain will contain information from both the LR and HR images, thereby enhancing the angular domain information. The specific details of MaskBlur are described in Sec. III-C.

C. MaskBlur

As shown in Fig. 4, our MaskBlur consists of spatial blur and angular dropout to generate new training samples.

Spatial Blur randomly generate a spatial mask M_{spa} for k -th SAI from \mathcal{L}_{LR} and utilize the spatial blur operation between \mathcal{L}_{LR} and \mathcal{L}_{HR} .

$$\begin{aligned}\hat{\mathcal{L}}_k^{LR \rightarrow HR} &= M_{\text{spa}} \odot \mathcal{L}_k^{LR} + (\mathbf{1} - M_{\text{spa}}) \odot \mathcal{L}_k^{HR \downarrow s} \\ \hat{\mathcal{L}}_k^{HR \rightarrow LR} &= M_{\text{spa}} \odot \mathcal{L}_k^{HR \downarrow s} + (\mathbf{1} - M_{\text{spa}}) \odot \mathcal{L}_k^{LR}\end{aligned}\quad (2)$$

where $\mathcal{L}_k^{HR \downarrow s}$ is achieved by downsampling the s ratio based on bilinear interpolation, $M_{\text{spa}} \in \{0, 1\}^{H \times W}$ denotes a binary mask indicating where to mask, $\mathbf{1}$ is a binary mask filled with ones, and \odot is the element-wise multiplication.

Angular Dropout randomly generate an angular mask M_{ang} for all views of LF and carry out the angular dropout operation.

$$\begin{aligned}\hat{\mathcal{L}}_k^{LR \rightarrow HR} &= \begin{cases} \hat{\mathcal{L}}_k^{LR \rightarrow HR}, & \text{if } M_{\text{ang}}[k] == 1 \\ \mathcal{L}_k^{LR}, & \text{if } M_{\text{ang}}[k] == 0 \end{cases}, k \in [1, UV] \\ \hat{\mathcal{L}}_k^{HR \rightarrow LR} &= \begin{cases} \hat{\mathcal{L}}_k^{HR \rightarrow LR}, & \text{if } M_{\text{ang}}[k] == 1 \\ \mathcal{L}_k^{LR}, & \text{if } M_{\text{ang}}[k] == 0 \end{cases}, k \in [1, UV]\end{aligned}\quad (3)$$

where $M_{\text{ang}} \in \{0, 1\}^{UV}$ denotes an angular binary mask representing which views are selected to perform the spatial blur, and UV indicates the angular number. Therefore, we can generate a new pair training sample $\{\hat{\mathcal{L}}^{LR \rightarrow HR}, \hat{\mathcal{L}}^{HR \rightarrow LR}\}$ through the spatial blur and angular dropout operations for each SAI from \mathcal{L}_{LR} . The procedure of MaskBlur is summarized in Algorithm 1. Note that our MaskBlur is a more generalized form than the CutBlur. When the spatial mask forms a single continuous rectangle and the angular mask is filled with ones, the MaskBlur is equivalent to the CutBlur.

D. Further Visual Analysis

There may be various degrees of blur in the real LF image. MaskBlur aims to enable the model to treat pixels differently when super-resolving LF images rather than blindly treating all pixels equally. To verify this, we perform the mask blur on some regions of the input LR image. We input blurred images into ATO [21] and ATO-Maskblur models respectively, and the results are shown in Fig. 5. The residual intensity map has significantly decreased in the model trained with MaskBlur. When the SR model takes the blurred image at the test phase,

Algorithm 1 MaskBlur algorithm

Input: LR LF image patch \mathcal{L}_{LR} , HR LF image patch \mathcal{L}_{HR} , DA probability p , spatial mask ratio s_r , spatial mask block-wise size s_{size} , angular mask ratio a_r .

Output: $\mathcal{L}_{LR}, \mathcal{L}_{HR}$

```

1:  $M_{\text{spa}} = \text{spa\_mask}(s_r, s_{\text{size}})$ .
2:  $M_{\text{ang}} = \text{ang\_mask}(a_r)$ .reshape(1, UV).
3: if Rand(0, 1) <  $p$  then
4:   for  $k = 1$  to  $UV$  do
5:     // Angular Dropout
6:     if  $M_{\text{ang}}[k] == 1$  then
7:       // Spatial Blur
8:       if Rand(0, 1) > 0.5 then
9:          $\mathcal{L}_k^{LR} = M_{\text{spa}} \odot \mathcal{L}_k^{LR} + (\mathbf{1} - M_{\text{spa}}) \odot \mathcal{L}_k^{HR \downarrow s}$ 
10:        {LR  $\rightarrow$  HR}
11:      else
12:         $\mathcal{L}_k^{LR} = M_{\text{spa}} \odot \mathcal{L}_k^{HR \downarrow s} + (\mathbf{1} - M_{\text{spa}}) \odot \mathcal{L}_k^{LR}$ 
13:        {HR  $\rightarrow$  LR}
14:      end if
15:    end if
16:  end for
17: end if
18: return  $\mathcal{L}_{LR}, \mathcal{L}_{HR}$ 

```

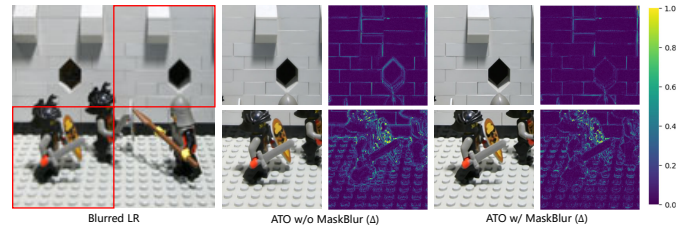


Fig. 5. Qualitative comparison of the ATO [21] with and without MaskBlur when the network inputs the mask blurred image during the inference. Red boxes indicate the regions of the spatial mask. Δ is the absolute residual intensity map between the network output and the ground-truth HR image. MaskBlur successfully generates clear results in more blurred areas (red boxes) while the ATO generates unrealistic artifacts.

it commonly produces overly blurred predictions, especially in areas with lines. MaskBlur can resolve this issue by directly providing such examples to the model during the training phase. Therefore, the models trained with MaskBlur enable discriminatively applying SR to the image.

E. Discussion

MaskBlur consists of spatial blur and angular dropout controlled by spatial and angular masks, respectively. Naturally, we need to discuss how to generate spatial masks and angular masks. For the spatial mask, we need to consider which mask sampling strategy to use, e.g., rectangular sampling [19], [20], grid sampling, or random sampling [41], [44], as shown in Fig. 6. Additionally, we also need to discuss the impact of block-wise size on the spatial mask. Specifically, when generating the spatial mask, we find that using image blocks (or patches) instead of pixels as the minimum unit of the mask can yield better results as it preserves the local completeness of the information. Regarding the angular mask, we continue to

consider which sampling strategy to use, e.g., grid or random. LF SAIs are stacked into different view stacks along four specific directions, namely horizontal, vertical, main diagonal, and anti-diagonal. These specific directions capture the implicit geometric information of the LF image, which has been proven to be crucial in tasks like LF depth estimation [53], [54] and SR [37]. Therefore, we also explore the performance of the angular mask on SAIs in different directions and their combinations (see Fig. 7). Angular dropout can also be combined with other spatial data augmentation strategies to further improve performance. Furthermore, we investigate the probabilities of MaskBlur, spatial mask, and angular mask, as well as the performance of MaskBlur with different dataset sizes. Detailed experimental results and analyses are presented in Sec. IV-B.

IV. EXPERIMENTS

A. Experimental Settings

Dataset and evaluation. Following the experimental settings of previous works [5], [36], we utilize five prevalent LF image datasets: EPFL [55], HCInew [56], HCIold [23], INRIA [57], and STFgantry [58], for both model training and testing based on BasicLFSR¹. Specifically, the angular resolution of each LF image is 9×9 , and we extract the central 5×5 SAIs for performing the SR task. The LF images are converted to the YCbCr color space, and the model performs SR on the Y channel. The Cb and Cr channels are upsampled using bicubic interpolation. For evaluation, we employ the PSNR and SSIM [59] metrics on the Y channel as the main metric on several benchmarks. Each dataset consists of multiple test scenes. We first calculate the metric scores for each scene by averaging the scores of all SAIs individually. Then, we compute the average score for the dataset by averaging the scores across multiple scenes. Finally, we obtain the overall average score by averaging the scores across all datasets.

Implementation details. We select five well-known LF image SR models, i.e., InterNet [36], ATO [21], IINet [2], DistgSSR [12] and EPIT [22] as baseline models to evaluate the generalization of MaskBlur, since these models differ significantly in terms of architecture and size. For a fair comparison, we train the baseline models with and without MaskBlur from scratch, following the recommended configurations provided by the authors’ code. During training, we randomly crop LF images into 128×128 image patches and downsample these patches using bicubic interpolation with a scale factor of 4, resulting in LR LF patches of size 32×32 , which serve as inputs to the $4 \times$ SR models. We employ the Adam optimizer with a batch size of 8 and a learning rate of $2e-4$, which is halved every 15 epochs. The default DA strategy is conducted by random 90-degree rotation and flipping in horizontal and vertical directions. The training of these baseline models is implemented in PyTorch and conducted on an NVIDIA A100 GPU.

¹<https://github.com/ZhengyuLiang24/BasicLFSR>

TABLE I
SPATIAL BLUR ABLATION EXPERIMENTS WITH INTERNET [36] IN $4 \times$ SR TASK ON BENCHMARK DATASETS. WE REPORT THE AVERAGE PSNR (DB, \uparrow) AND δ INDICATES THE PERFORMANCE GAP FROM THE BASELINE. DEFAULT SETTINGS ARE MARKED IN GRAY.

Spa. mask samp.	ratio	block	PSNR (δ)
InterNet-base	-	-	31.596 (+0.000)
rectangle	50%	4	31.635 (+0.039)
grid	50%	4	31.640 (+0.044)
learning	auto	4	31.653 (+0.057)
random	50%	4	31.651 (+0.055)
random	50%	1	31.623 (+0.027)
random	50%	2	31.626 (+0.030)
random	50%	4	31.651 (+0.055)
random	50%	8	31.636 (+0.040)
random	50%	16	31.628 (+0.032)
random	25%	4	31.633 (+0.037)
random	50%	4	31.651 (+0.055)
random	75%	4	31.602 (+0.006)

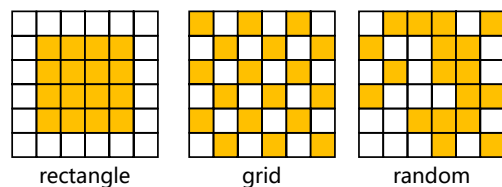


Fig. 6. Illustration of three different spatial mask sampling strategies: rectangle, grid, and random (default).

B. Ablation Study

Spatial mask sampling strategy. Given a masking ratio of 0.5, we compare three different mask sampling strategies: rectangle sampling, grid sampling, and random sampling, as illustrated in Fig. 6. Table I presents the comparative results of these sampling strategies, indicating that all three sampling strategies significantly outperform the baseline, demonstrating the effectiveness of spatial blur. Among them, random sampling performs the best, and we conduct further analysis. Rectangle sampling leads to a significant loss of information in the sampled central region, making it challenging for the model to learn effectively. Grid sampling performs better than rectangle sampling due to reduced information loss around each patch. However, due to the fixed sampling patches, its representational quality is relatively low. Random sampling involves randomly selecting image patches to form the mask region, which not only has less information loss but also has the strongest representation. It serves as a general sampling strategy, with rectangle sampling and grid sampling as special cases. We also conducted a comparative analysis of the random sampling strategy and the learning-based approach. Specifically, we employ two convolutional layers with sigmoid activation to automatically generate the spatial mask for spatial blur. The results indicate that while the learning-based approach offers minimal improvement over the random sampling strategy, it introduces additional parameters and computational effort, slowing the training speed by about three minutes per epoch compared to the random sampling strategy. In contrast,

TABLE II
ANGULAR DROPOUT ABLATION EXPERIMENTS WITH INTERNET [36] IN $4\times$ SR TASK ON BENCHMARK DATASETS. WE REPORT THE AVERAGE PSNR (DB, \uparrow) AND δ INDICATES THE PERFORMANCE GAP FROM THE BASELINE. DEFAULT SETTINGS ARE MARKED IN GRAY.

Angular mask sampling	ratio	PSNR (δ)
InterNet-base	-	31.596 (+0.000)
InterNet+spatial blur	-	31.651 (+0.055)
grid	76%	31.658 (+0.062)
horizontal	80%	31.656 (+0.060)
vertical	80%	31.661 (+0.065)
main diagonal	80%	31.658 (+0.062)
antidiagonal	80%	31.668 (+0.072)
cross	64%	31.668 (+0.072)
bidiagonal	64%	31.669 (+0.073)
cross+bidiagonal	32%	31.671 (+0.075)
random	75%	31.732 (+0.136)
random	25%	31.676 (+0.080)
random	50%	31.703 (+0.097)
random	75%	31.732 (+0.136)

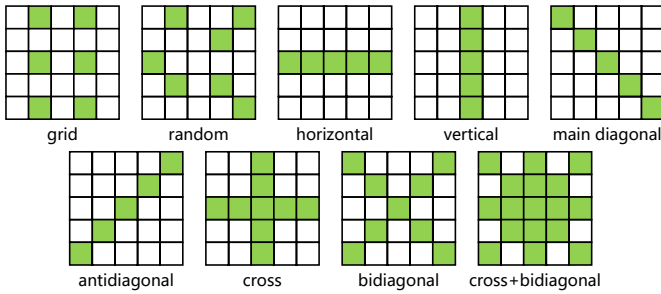


Fig. 7. Illustration of different angular mask sampling strategies: rectangle, random (default), and special direction and combinations.

the InterNet model trained with the random sampling strategy only experiences an increase of approximately one minute per epoch. Therefore, the random sampling strategy provides a better trade-off between performance and computational efficiency.

Spatial mask block-wise size. We investigate the impact of the block-wise size of the spatial mask while using training image patches of size 32×32 . As evident from Table I, a minimal block-wise size can disrupt the local completeness of information, while a tremendous block-wise size results in increased information loss, e.g., the information all comes from the LR domain, making it difficult for the model to learn. Our experiments determined that a block-wise size of 4 is optimal, as it strikes a balance between local completeness and information loss.

Spatial mask ratio. We investigate the impact of the spatial mask ratio. Table I presents the results for different spatial masking ratios, with a ratio of 50% yielding the best performance. Our analysis suggests that when the masking ratio is either too high or too low, the new training samples contain only a small portion of either LR or HR information, leading to suboptimal spatial DA. Therefore, a 50% ratio provides a balanced mix of LR and HR information in the new training samples, resulting in the most effective spatial DA.

Angular mask sampling strategy. We analyze some factors

TABLE III
ANGULAR DROPOUT COMBINED WITH OTHER SPATIAL DA STRATEGIES WITH INTERNET [36] IN $4\times$ SR TASK ON BENCHMARK DATASETS. δ INDICATES THE PERFORMANCE GAP FROM THE BASELINE.

DA strategy	δ
RGB permute	+0.009
Cutout	+0.001
Mixup	+0.025
CutBlur	+0.033
saptial blur	+0.055
RGB permute+angular dropout	+0.042
Cutout+angular dropout	+0.049
Mixup+angular dropout	+0.045
CutBlur+angular dropout	+0.087
spatial blur+angular dropout (MaskBlur)	+0.136

TABLE IV
DA PROBABILITY p ABLATION EXPERIMENTS WITH INTERNET [36] IN $4\times$ SR TASK ON BENCHMARK DATASETS. WE REPORT THE AVERAGE PSNR (DB, \uparrow) AND δ INDICATES THE PERFORMANCE GAP FROM THE BASELINE. DEFAULT SETTINGS ARE MARKED IN GRAY.

Method	p	PSNR (δ)
InterNet-base	0.00	31.596 (+0.000)
+MaskBlur	0.25	31.732 (+0.136)
+MaskBlur	0.50	31.697 (+0.101)
+MaskBlur	0.75	31.652 (+0.056)
+MaskBlur	1.00	31.679 (+0.083)

that affect angular dropout. Similar to spatial mask sampling strategies, we first investigate different angular mask sampling strategies, i.e., grid sampling and random sampling, as shown in Fig. 7. From Table II, we observe that both sampling strategies can further improve performance based on spatial blur, with random sampling achieving greater improvement. Furthermore, we design special angular masks composed of different angular directions and their combinations, i.e., horizontal, vertical, main diagonal, and antidiagonal, as shown in Fig. 7. Table II demonstrates that the effectiveness of special angular masks is significantly lower compared to random sampling, which indicates that special angular masks have little impact on angular dropout.

Angular mask ratio. The angular masking ratio also affects the performance of angular dropout, so we explore various ratios to understand their impact. As shown in Table II, the optimal performance is achieved when the ratio is set to 75%, indicating that when 75% of the views are dropped out while the remaining 25% undergo spatial blur, the performance is optimal. The finding differs from the spatial domain, suggesting that retaining a higher proportion of LR information during the DA process is crucial in the angular domain.

Angular dropout combined with other spatial DA strategies. Our MaskBlur consists of two separate operations: spatial blur and angular dropout. Therefore, angular dropout can also be combined with other spatial DA strategies. We compare several general spatial DA strategies combined with angular dropout, i.e., RGB permute, Cutout [39], Mixup [38], and CutBlur [19]. From Table III, we can find that while the general spatial DA strategies can improve the performance of the baseline model, their impact is comparatively modest and

TABLE V
VARIOUS DATASET SIZES ABLATION EXPERIMENTS WITH INTERNET [36] IN $4\times$ SR TASK ON BENCHMARK DATASETS. WE REPORT THE AVERAGE PSNR (DB, \uparrow) AND δ INDICATES THE PERFORMANCE GAP FROM THE BASELINE. DEFAULT SETTINGS ARE MARKED IN GRAY .

Method	Data Size	PSNR (δ)
InterNet-base	25%	30.903 (+0.000)
+MaskBlur	25%	31.104 (+0.201)
InterNet-base	50%	31.175 (+0.000)
+MaskBlur	50%	31.349 (+0.174)
InterNet-base	75%	31.460 (+0.000)
+MaskBlur	75%	31.616 (+0.156)
InterNet-base	100%	31.596 (+0.000)
+MaskBlur	100%	31.732 (+0.136)

TABLE VI
COMPREHENSIVE COMPARISON OF ATO [21] AND INTERNET [36] COMBINED WITH DIFFERENT DA STRATEGIES IN SR $4\times$ TASKS ON FIVE BENCHMARK DATASETS. WE REPORT THE AVERAGE METRIC IN TERMS OF PSNR (DB, \uparrow) AND SSIM (\uparrow), WHERE δ INDICATES THE PERFORMANCE GAP FROM THE BASELINE. THE TRAINING TIME PER EPOCH IS ALSO REPORTED TO REPRESENT THE COMPUTATION COST. OUR RESULTS ARE MARKED IN GRAY .

Method	Training Time	Avg. PSNR (δ)	Avg. SSIM (δ)
ATO-base	27 min	31.494 (+0.000)	0.9384 (+0.0000)
ATO-CutBlur	29 min	31.576 (+0.072)	0.9387 (+0.0003)
ATO-CutMIB	29 min	31.646 (+0.142)	0.9390 (+0.0006)
ATO-MaskBlur	29 min	31.872 (+0.378)	0.9401 (+0.0017)
InterNet-base	14 min	31.596 (+0.000)	0.9374 (+0.0000)
InterNet-CutBlur	15 min	31.629 (+0.033)	0.9381 (+0.0007)
InterNet-CutMIB	15 min	31.664 (+0.068)	0.9389 (+0.0015)
InterNet-MaskBlur	15 min	31.732 (+0.136)	0.9404 (+0.0030)

falls short of the improvement achieved by spatial blur alone. Moreover, when these spatial DA strategies are combined with angular dropout, the improvement becomes notably more substantial. This result underscores the broad applicability and generalization of our angular dropout.

DA probability. DA probability p determines the ratio of samples trained with MaskBlur. We conduct experiments to choose DA probability p under the condition that the spatial mask and angular mask adopt the random sampling strategy, spatial mask block-wise size is set to 4, the spatial masking ratio is set to 0.5, and the angular masking ratio is set to 0.75. Table IV shows that the model can achieve the highest PSNR at $p = 0.25$. We analyze some differences between the augmented sample distribution and the original sample distribution. Therefore, a high proportion of DA will destroy the original image distribution, resulting in sub-optimal results, while using a low proportion of DA can simultaneously maintain the original sample distribution and increase the training sample, resulting in better results.

Various dataset size. We further investigate the model performance under different dataset sizes, as shown in Table V. We conduct experiments with 100%, 75%, 50%, and 25% of the dataset size, respectively. First, our method brings great improvements to the Internet in various settings. As the ratio of the dataset decreases, the performance gap between the baseline and our method widens. When the dataset ratio is

less than 50%, our method demonstrates an improvement of up to 0.201 dB. In addition, when trained with MaskBlur, the InterNet trained on 75% of the dataset outperforms the 100% baseline. This proves the effectiveness of our method.

C. Quantitative Comparisons

We compare MaskBlur with state-of-the-art (SOTA) DA strategies for SR, i.e., CutBlur [19] and CutMIB [20], on various benchmark datasets. The results are shown in Tables VII and VI. Both CutBlur and CutMIB strategies improve the average PSNR of the baseline methods, except for a slight performance decrease on a few individual datasets. We further analyzed the reason for the poor performance of EPIT-CutBlur where CutBlur applies data augmentation solely in the spatial domain without considering the angular domain. CutBlur degrades the quality of the EPI subspace significantly, thereby increasing the difficulty for EPIT to learn the spatial-angular correlations within the EPI subspace, leading to sub-optimal performance. As observed in Tables VII and VI, compared to MaskBlur, CutBlur and CutMIB have limited improvements to the models. For instance, the ATO model trained with MaskBlur achieves an average PSNR improvement of **0.378 dB** compared to the baseline. The improvement with CutBlur and CutMIB is only 0.072 dB and 0.142 dB, respectively. The InterNet trained with MaskBlur achieves an average gain of **0.0030** in terms of SSIM than CutBlur (0.0007) and CutMIB (0.0015). We also compared the computational costs with other DA schemes, as shown in Table VI. While MaskBlur is comparable to CutBlur and CutMIB in terms of computational costs, it significantly outperforms them in terms of performance. The computational overhead introduced by MaskBlur during training is minimal. For instance, when applied to the InterNet model, the training time per epoch increases by approximately 1 minute. This slight increase in training time is worthwhile considering the performance improvements MaskBlur provides. Importantly, MaskBlur is only executed during the training phase. Therefore, it does not add any computational overhead during the inference phase. When combined with other SR methods, MaskBlur demonstrates superior overall performance compared to CutBlur and CutMIB, confirming the effectiveness of our approach.

D. Qualitative Comparisons

We also qualitatively compare the results of various baseline models with and without MaskBlur on $4\times$ LF image SR task, as shown in Fig. 8. Firstly, we can observe a noticeable improvement in spatial visual quality when using the MaskBlur DA strategy, e.g., the ruling lines appear clearer. Secondly, the EPI images with MaskBlur exhibit clear pixel slopes, reflecting the ability of our method to maintain angular consistency. Furthermore, following previous methods [12], [20], we apply a depth estimation algorithm, i.e., SPO [60] to the super-resolved LF images, and the results are shown in Fig. 9. The depth maps obtained employing the MaskBlur strategy show smaller average errors ($\text{MSE} \times 100$) and provide more accurate estimations in some edge regions. This further demonstrates that our MaskBlur can maintain angular consistency.

TABLE VII

QUANTITATIVE DETAILED COMPARISON OF VARIOUS SR METHODS COMBINED WITH DIFFERENT DA STRATEGIES IN SR $4\times$ TASKS ON BENCHMARK DATASETS. WE REPORT THE AVERAGE PSNR (dB, \uparrow) AND δ INDICATES THE PERFORMANCE GAP FROM THE BASELINE.

Method	EPFL	HCInew	HCIold	INRIA	STFgantry	Average
	PSNR (δ)	PSNR (δ)	PSNR (δ)	PSNR (δ)	PSNR (δ)	PSNR (δ)
ATO-base	28.515 (+0.000)	30.813 (+0.000)	36.893 (+0.000)	30.677 (+0.000)	30.573 (+0.000)	31.494 (+0.000)
ATO-CutBlur	28.612 (+0.097)	30.896 (+0.083)	36.991 (+0.098)	30.798 (+0.121)	30.585 (+0.012)	31.576 (+0.072)
ATO-CutMIB	28.631 (+0.116)	30.950 (+0.138)	37.050 (+0.157)	30.829 (+0.152)	30.771 (+0.198)	31.646 (+0.142)
ATO-MaskBlur	28.893 (+0.378)	31.075 (+0.262)	37.274 (+0.381)	31.089 (+0.412)	31.027 (+0.454)	31.872 (+0.378)
InterNet-base	28.687 (+0.000)	31.011 (+0.000)	37.109 (+0.000)	30.658 (+0.000)	30.514 (+0.000)	31.596 (+0.000)
InterNet-CutBlur	28.845 (+0.158)	30.980 (-0.031)	37.149 (+0.040)	30.800 (+0.142)	30.371 (-0.143)	31.629 (+0.033)
InterNet-CutMIB	28.856 (+0.169)	31.009 (-0.002)	37.184 (+0.075)	30.813 (+0.155)	30.460 (-0.054)	31.664 (+0.068)
InterNet-MaskBlur	28.811 (+0.124)	31.108 (+0.097)	37.331 (+0.222)	30.733 (+0.075)	30.679 (+0.165)	31.732 (+0.136)
IINet-base	29.005 (+0.000)	31.313 (+0.000)	37.547 (+0.000)	31.086 (+0.000)	31.198 (+0.000)	32.030 (+0.000)
IINet-CutBlur	29.046 (+0.041)	31.357 (+0.044)	37.595 (+0.048)	31.026 (-0.060)	31.300 (+0.102)	32.065 (+0.035)
IINet-CutMIB	29.106 (+0.101)	31.422 (+0.109)	37.613 (+0.066)	31.089 (+0.003)	31.450 (+0.252)	32.136 (+0.106)
IINet-MaskBlur	29.115 (+0.110)	31.363 (+0.050)	37.711 (+0.164)	31.116 (+0.030)	31.395 (+0.197)	32.140 (+0.110)
DistgSSR-base	29.015 (+0.000)	31.410 (+0.000)	37.588 (+0.000)	31.015 (+0.000)	31.635 (+0.000)	32.133 (+0.000)
DistgSSR-CutBlur	29.023 (+0.008)	31.418 (+0.008)	37.599 (+0.011)	31.022 (+0.007)	31.638 (+0.003)	32.140 (+0.007)
DistgSSR-CutMIB	29.034 (+0.019)	31.445 (+0.035)	37.618 (+0.030)	31.030 (+0.015)	31.681 (+0.046)	32.162 (+0.029)
DistgSSR-MaskBlur	29.282 (+0.267)	31.453 (+0.043)	37.656 (+0.068)	31.304 (+0.289)	31.702 (+0.067)	32.279 (+0.146)
EPIT-base	29.317 (+0.000)	31.510 (+0.000)	37.679 (+0.000)	31.352 (+0.000)	32.180 (+0.000)	32.408 (+0.000)
EPIT-CutBlur	29.288 (-0.029)	31.504 (-0.006)	37.677 (-0.002)	31.287 (-0.065)	32.175 (-0.005)	32.386 (-0.022)
EPIT-CutMIB	29.309 (-0.008)	31.514 (+0.004)	37.681 (+0.002)	31.332 (-0.020)	32.192 (+0.012)	32.406 (-0.002)
EPIT-MaskBlur	29.328 (+0.011)	31.528 (+0.018)	37.703 (+0.024)	31.384 (+0.032)	32.202 (+0.004)	32.429 (+0.021)



Fig. 8. Qualitative comparisons of various SR models trained with and without the MaskBlur $4\times$ LF image SR. # denotes that the networks are trained with the MaskBlur. We report the PSNR (dB, \uparrow). Please zoom in for better visualization.

E. Applications

LF image denoising. We extend MaskBlur to the LF image denoising task. Following [62], [63], we utilize the same noise generation strategy to create the HCInew [56] dataset for training and testing. Specifically, we add zero-mean Gaussian noise with different standard deviations ($\sigma = 10, 20, 50$) to the LF images to generate the noisy images. Next, we remove

the upsampling operation from the SR models and retrain the ATO, InterNet, IINet, and DistgSSR models for different noise levels. Table VIII presents the quantitative results with and without the MaskBlur DA strategy. We can observe that MaskBlur consistently improves the PSNR performance of the baseline models across different noise settings. As shown in Fig. 10, the denoised images with MaskBlur exhibit less noise

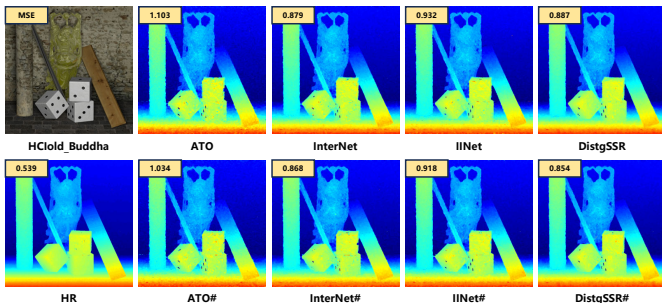


Fig. 9. Depth estimation results achieved by SPO [60] using $4\times$ SR LF images produced by different SR methods trained with and without the MaskBlur. # denotes that the networks are trained with the MaskBlur. We report the mean square error multiplied by 100 (MSE \times 100), lower is better.

TABLE VIII

QUANTITATIVE COMPARISON OF VARIOUS METHODS FOR LF IMAGE DENOISING TASK WITH DIFFERENT NOISE LEVELS ON HCINew [56]. WE REPORT THE AVERAGE PSNR (dB, \uparrow) AND δ INDICATES THE PERFORMANCE GAP FROM THE BASELINE. THE MODELS TRAINED WITH MASKBLUR ARE MARKED IN GRAY .

Method	$\sigma = 10$	$\sigma = 20$	$\sigma = 50$
	PSNR (δ)	PSNR (δ)	PSNR (δ)
ATO	38.422 (+0.000)	35.152 (+0.000)	31.343 (+0.000)
+MaskBlur	38.546 (+0.124)	35.281 (+0.129)	31.535 (+0.192)
InterNet	38.260 (+0.000)	35.493 (+0.000)	31.980 (+0.000)
+MaskBlur	38.560 (+0.300)	35.548 (+0.055)	32.090 (+0.110)
IINet	39.526 (+0.000)	36.466 (+0.000)	32.258 (+0.000)
+MaskBlur	39.566 (+0.040)	36.512 (+0.046)	32.324 (+0.066)
DistgSSR	39.662 (+0.000)	36.617 (+0.000)	32.449 (+0.000)
+MaskBlur	39.785 (+0.123)	36.630 (+0.013)	32.496 (+0.047)

TABLE IX

QUANTITATIVE COMPARISON OF VARIOUS METHODS FOR LF IMAGE DEBLURRING TASK WITH DIFFERENT BLUR KERNELS ON HCINew [56]. WE REPORT THE AVERAGE PSNR (dB, \uparrow) AND δ INDICATES THE PERFORMANCE GAP FROM THE BASELINE. THE MODELS TRAINED WITH MASKBLUR ARE MARKED IN GRAY .

Method	isotropic	anisotropic	motion
	PSNR (δ)	PSNR (δ)	PSNR (δ)
ATO	30.018 (+0.000)	30.947 (+0.000)	23.450 (+0.000)
+MaskBlur	30.170 (+0.152)	31.027 (+0.080)	23.651 (+0.201)
InterNet	30.709 (+0.000)	29.678 (+0.000)	23.040 (+0.000)
+MaskBlur	31.027 (+0.318)	29.872 (+0.194)	23.127 (+0.087)
IINet	31.652 (+0.000)	30.849 (+0.000)	23.335 (+0.000)
+MaskBlur	32.009 (+0.357)	31.119 (+0.270)	23.455 (+0.120)
DistgSSR	32.776 (+0.000)	31.287 (+0.000)	24.131 (+0.000)
+MaskBlur	32.908 (+0.132)	31.332 (+0.045)	24.656 (+0.039)

and clearer lines than those without MaskBlur.

LF image deblurring. We evaluate the effectiveness of MaskBlur on the LF image deblurring task. Specifically, we synthesize blurred images using isotropic Gaussian kernel, anisotropic Gaussian blur, and motion blur. Similar to LF image denoising, we retrain the ATO, InterNet, IINet, and DistgSSR models for different blur types on the HCInew [56] dataset. Table IX presents the quantitative results for

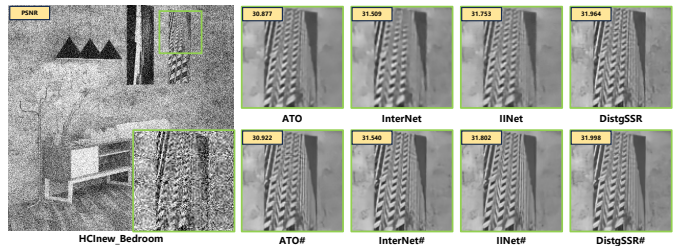


Fig. 10. Visual comparisons of various models trained with and without MaskBlur on the $\sigma = 50$ LF denoising task. We report the PSNR (dB, \uparrow) on the top-left.

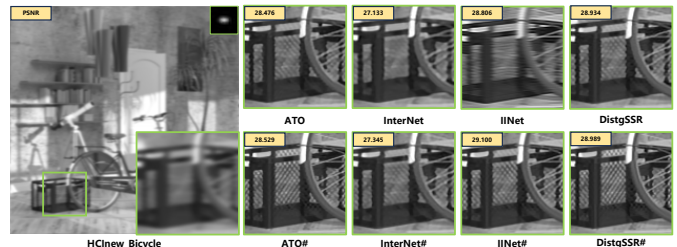


Fig. 11. Visual comparisons of various models with and without MaskBlur on LF deblurring under the anisotropic Gaussian blur. We report the PSNR (dB, \uparrow) on the top-left.

the three different types of blur kernels. We can observe that the models trained with the MaskBlur strategy achieve better PSNR results. We also visualize the deblurring results in Figure 11, and it can be seen that the deblurred images generated by the models trained with MaskBlur effectively reduce blur and improve the visual quality of the views.

LF image low-light enhancement. We also compare MaskBlur with other DA schemes, i.e., CutBlur [19] and CutMIB [20], for the task of LF image low-light enhancement. Specifically, inspired by [64]–[66], we synthesize low-light LF images using different level gamma correction ($\gamma = 0.2, 0.3, 0.5$) and add zero-mean Gaussian noise with deviations ($\sigma = 10$). We conduct experiments on the HCInew [56] dataset using the InterNet [36] and DistgSSR [12]. Table X shows the quantitative comparison results, demonstrating that training InterNet and DistgSSR with MaskBlur performs better than other DA schemes. Additionally, as shown in Fig. 12, models trained with the MaskBlur produce clearer edges and textures, further proving the generalization capability of the MaskBlur scheme.

Real-world LF image SR. Most existing LF image SR methods employ bicubic interpolation to simulate the degradation between HR and LR. However, the degradation of real-world LF images is very complicated. The mathematical equation of the classical degradation model [17], [67] is given below.

$$\mathcal{I}_i^{LR} = (\mathcal{I}_i^{HR} \otimes k_i) \downarrow_s + n_i \quad (4)$$

where \otimes represents convolution operation, k_i is a Gaussian blur kernel, \downarrow_s is the downsampling operation with scale factor s , and n_i represents Gaussian noise. Bicubic degradation can be considered a special case of classical degradation as it can be approximated by setting an appropriate zero-noise kernel

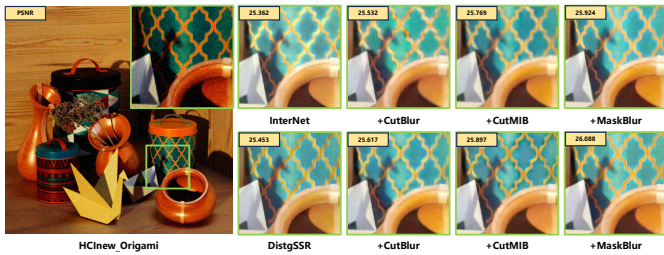


Fig. 12. Visual comparisons of various models trained with different DA schemes on the $\gamma = 0.3$ LF low-light enhancement task. We report the PSNR (dB, \uparrow) on the top-left.

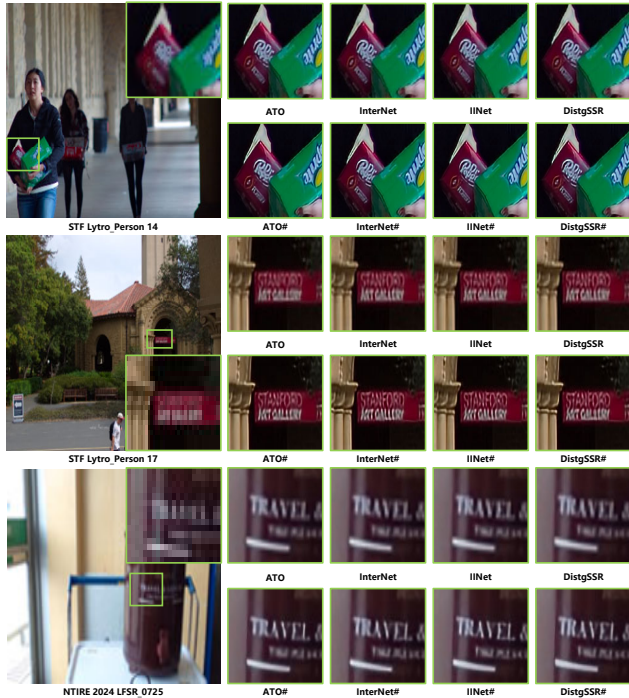


Fig. 13. Visual comparisons of various models with and without MaskBlur on real-world scenes from STF Lytro [61] and NTIRE 2024 LFSR validation set [18]

[68], [69]. Various factors, such as blur kernel and noise level influence the degradation model.

We employ the classical degradation model to simulate real scene degradation and evaluate the generalization of our method in real-world LF image SR task on EPFL [55] since the dataset contains real-world scenes captured by a Lytro Illum LF camera. Specifically, we directly utilize the baseline networks, i.e., InterNet [36], ATO [21], IINet [2], DistgSSR [12], and their corresponding versions trained with MaskBlur to conduct real-world SR. Note that we only consider isotropic Gaussian blur kernel, with each view being assigned the same degenerate kernel, and noise is not considered. Following the setting in [70], [71], the kernel size is set to 21 and the kernel width is set to 1.8, 2.5, and 3.2 for evaluation. As shown in Table XI, various models trained with MaskBlur consistently exhibit performance improvements across different Gaussian blur kernels. This underscores the generalization ability of our method in the real-world LF image SR task.

TABLE X

QUANTITATIVE COMPARISON OF VARIOUS METHODS TRAINED WITH DIFFERENT DA SCHEMES IN LF IMAGE LOW-LIGHT ENHANCEMENT TASK UNDER DIFFERENT GAMMA CORRECTION ON HCINEW [56]. WE REPORT THE AVERAGE PSNR (dB, \uparrow) AND δ INDICATES THE PERFORMANCE GAP FROM THE BASELINE. THE MODELS TRAINED WITH MASKBLUR ARE MARKED IN GRAY.

Method	$\gamma = 0.2$	$\gamma = 0.3$	$\gamma = 0.5$
	PSNR (δ)	PSNR (δ)	PSNR (δ)
InterNet	24.222 (+0.000)	28.898 (+0.000)	33.161 (+0.000)
+CutBlur	24.284 (+0.062)	28.942 (+0.044)	33.185 (+0.024)
+CutMIB	24.353 (+0.131)	29.014 (+0.116)	33.211 +0.050
+MaskBlur	24.575 (+0.353)	29.121 (+0.223)	33.285 (+0.124)
DistgSSR	25.526 (+0.000)	29.480 (+0.000)	34.804 (+0.000)
+CutBlur	25.530 (+0.004)	29.492 (+0.012)	34.814 (+0.010)
+CutMIB	25.632 (+0.106)	29.598 (+0.118)	34.920 (+0.116)
+MaskBlur	25.821 (+0.295)	29.673 (+0.193)	34.959 (+0.155)

TABLE XI

QUANTITATIVE COMPARISON OF VARIOUS METHODS IN REAL-WORLD LF IMAGE $4\times$ SR TASK UNDER DIFFERENT ISOTROPIC GAUSSIAN KERNELS ON EPFL [55]. WE REPORT THE AVERAGE PSNR (dB, \uparrow) AND δ INDICATES THE PERFORMANCE GAP FROM THE BASELINE. THE MODELS TRAINED WITH MASKBLUR ARE MARKED IN GRAY.

Method	$k = 1.8$	$k = 2.5$	$k = 3.2$
	PSNR (δ)	PSNR (δ)	PSNR (δ)
ATO	25.084 (+0.000)	23.630 (+0.000)	22.638 (+0.000)
+MaskBlur	25.096 (+0.012)	23.651 (+0.021)	22.658 (+0.020)
InterNet	25.168 (+0.000)	23.646 (+0.000)	22.638 (+0.000)
+MaskBlur	25.149 (+0.002)	23.666 (+0.020)	22.656 (+0.018)
IINet	25.165 (+0.000)	23.650 (+0.000)	22.634 (+0.000)
+MaskBlur	25.171 (+0.006)	23.652 (+0.002)	22.645 (+0.011)
DistgSSR	25.111 (+0.000)	23.650 (+0.000)	22.641 (+0.000)
+MaskBlur	25.151 (+0.040)	23.665 (+0.015)	22.651 (+0.010)

Furthermore, we compare different methods trained with and without the MaskBlur on real-world LF images taken with a Lytro Illum camera from STF Lytro [61] and NTIRE 2024 LFSR validation set [18]. Since there is no ground truth available for real-world scenes, we perform a visual comparison. Figure 13 shows that the models with the MaskBlur strategy generate better detail preservation and visual effects, which demonstrates the great generalization ability of our MaskBlur.

V. CONCLUSION

This paper has proposed a novel DA strategy, MaskBlur, for LF image SR, utilizing both spatial and angular masks. The spatial mask dictates where pixels undergo blurring, while the angular mask determines which views are dropped. MaskBlur encourages the model to adaptively treat pixels differently in the spatial and angular domains during LF image SR. The effectiveness of MaskBlur is demonstrated through notable performance improvements in existing SR models. Furthermore, we validate the generalization of MaskBlur in LF image denoising, deblurring, low-light enhancement, and real-world SR tasks. Looking ahead, our future work will explore the application of MaskBlur for video-related tasks.

REFERENCES

- [1] V. K. Ghassab and N. Bouguila, "Light field super-resolution using edge-preserved graph-based regularization," *IEEE Transactions on Multimedia*, vol. 22, no. 6, pp. 1447–1457, 2019.
- [2] G. Liu, H. Yue, J. Wu, and J. Yang, "Intra-inter view interaction network for light field image super-resolution," *IEEE Transactions on Multimedia*, vol. 25, pp. 256–266, 2021.
- [3] Y. Sun, L. Li, Z. Li, S. Wang, S. Liu, and G. Li, "Learning a compact spatial-angular representation for light field," *IEEE Transactions on Multimedia*, 2022.
- [4] G. Liu, H. Yue, J. Wu, and J. Yang, "Efficient light field angular super-resolution with sub-aperture feature learning and macro-pixel upsampling," *IEEE Transactions on Multimedia*, 2022.
- [5] R. Cong, H. Sheng, D. Yang, Z. Cui, and R. Chen, "Exploiting spatial and angular correlations with deep efficient transformers for light field image super-resolution," *IEEE Transactions on Multimedia*, 2023.
- [6] Y. Wang, L. Wang, Z. Liang, J. Yang, W. An, and Y. Guo, "Occlusion-aware cost constructor for light field depth estimation," in *Proceedings of the IEEE/CVF Conference on Computer Vision and Pattern Recognition*, 2022, pp. 19 809–19 818.
- [7] H. Sheng, Y. Liu, J. Yu, G. Wu, W. Xiong, R. Cong, R. Chen, L. Guo, Y. Xie, S. Zhang *et al.*, "Lfnat 2023 challenge on light field depth estimation: Methods and results," in *Proceedings of the IEEE/CVF Conference on Computer Vision and Pattern Recognition Workshops*, 2023, pp. 3472–3484.
- [8] W. Chao, X. Wang, Y. Wang, G. Wang, and F. Duan, "Learning sub-pixel disparity distribution for light field depth estimation," *IEEE Transactions on Computational Imaging*, vol. 9, pp. 1126–1138, 2023.
- [9] G. Wu, Y. Wang, Y. Liu, L. Fang, and T. Chai, "Spatial-angular attention network for light field reconstruction," *IEEE Transactions on Image Processing*, vol. 30, pp. 8999–9013, 2021.
- [10] C. Kim, H. Zimmer, Y. Pritch, A. Sorkine-Hornung, and M. H. Gross, "Scene reconstruction from high spatio-angular resolution light fields," *ACM Transactions on Graphics (TOG)*, vol. 32, no. 4, pp. 73–1, 2013.
- [11] Z. Liang, Y. Wang, L. Wang, J. Yang, and S. Zhou, "Light field image super-resolution with transformers," *IEEE Signal Processing Letters*, vol. 29, pp. 563–567, 2022.
- [12] Y. Wang, L. Wang, G. Wu, J. Yang, W. An, J. Yu, and Y. Guo, "Disentangling light fields for super-resolution and disparity estimation," *IEEE Transactions on Pattern Analysis and Machine Intelligence*, 2022.
- [13] Z. Cheng, Y. Liu, and Z. Xiong, "Spatial-angular versatile convolution for light field reconstruction," *IEEE Transactions on Computational Imaging*, vol. 8, pp. 1131–1144, 2022.
- [14] Y. Chen, S. Zhang, S. Chang, and Y. Lin, "Light field reconstruction using efficient pseudo 4d epipolar-aware structure," *IEEE Transactions on Computational Imaging*, vol. 8, pp. 397–410, 2022.
- [15] V. Van Duong, T. N. Huu, J. Yim, and B. Jeon, "Light field image super-resolution network via joint spatial-angular and epipolar information," *IEEE Transactions on Computational Imaging*, vol. 9, pp. 350–366, 2023.
- [16] Y. Wang, L. Wang, Z. Liang, J. Yang, R. Timofte, Y. Guo *et al.*, "NTIRE 2023 challenge on light field image super-resolution: Dataset, methods and results," in *Proceedings of the IEEE/CVF Conference on Computer Vision and Pattern Recognition Workshops*, 2023, pp. 1320–1335.
- [17] Y. Wang, Z. Liang, L. Wang, J. Yang, W. An, and Y. Guo, "Real-world light field image super-resolution via degradation modulation," *IEEE Transactions on Neural Networks and Learning Systems*, 2024.
- [18] Y. Wang, Z. Liang, Q. Chen, L. Wang, J. Yang, R. Timofte, Y. Guo *et al.*, "Ntire 2024 challenge on light field image super-resolution: Methods and results," in *Proceedings of the IEEE/CVF Conference on Computer Vision and Pattern Recognition Workshops*, 2024.
- [19] J. Yoo, N. Ahn, and K.-A. Sohn, "Rethinking data augmentation for image super-resolution: A comprehensive analysis and a new strategy," in *Proceedings of the IEEE/CVF Conference on Computer Vision and Pattern Recognition*, 2020, pp. 8375–8384.
- [20] Z. Xiao, Y. Liu, R. Gao, and Z. Xiong, "Cutmib: Boosting light field super-resolution via multi-view image blending," in *Proceedings of the IEEE/CVF Conference on Computer Vision and Pattern Recognition*, 2023, pp. 1672–1682.
- [21] J. Jin, J. Hou, J. Chen, and S. Kwong, "Light field spatial super-resolution via deep combinatorial geometry embedding and structural consistency regularization," in *Proceedings of the IEEE/CVF conference on computer vision and pattern recognition*, 2020, pp. 2260–2269.
- [22] Z. Liang, Y. Wang, L. Wang, J. Yang, S. Zhou, and Y. Guo, "Learning non-local spatial-angular correlation for light field image super-resolution," in *Proceedings of the IEEE/CVF International Conference on Computer Vision*, 2023, pp. 12 376–12 386.
- [23] S. Wanner, S. Meister, and B. Goldluecke, "Datasets and benchmarks for densely sampled 4d light fields," in *VMV*, vol. 13. Citeseer, 2013, pp. 225–226.
- [24] T. He, Z. Zhang, H. Zhang, Z. Zhang, J. Xie, and M. Li, "Bag of tricks for image classification with convolutional neural networks," in *Proceedings of the IEEE/CVF conference on computer vision and pattern recognition*, 2019, pp. 558–567.
- [25] Z. Zhang, T. He, H. Zhang, Z. Zhang, J. Xie, and M. Li, "Bag of freebies for training object detection neural networks," *arXiv preprint arXiv:1902.04103*, 2019.
- [26] C.-K. Liang and R. Ramamoorthi, "A light transport framework for lenslet light field cameras," *ACM Transactions on Graphics (TOG)*, vol. 34, no. 2, pp. 1–19, 2015.
- [27] S. Wanner and B. Goldluecke, "Variational light field analysis for disparity estimation and super-resolution," *IEEE Transactions on Pattern Analysis and Machine Intelligence*, vol. 36, no. 3, pp. 606–619, 2013.
- [28] T. E. Bishop and P. Favaro, "The light field camera: Extended depth of field, aliasing, and superresolution," *IEEE transactions on pattern analysis and machine intelligence*, vol. 34, no. 5, pp. 972–986, 2011.
- [29] K. Mitra and A. Veeraraghavan, "Light field denoising, light field superresolution and stereo camera based refocussing using a gmm light field patch prior," in *2012 IEEE Computer Society Conference on Computer Vision and Pattern Recognition Workshops*. IEEE, 2012, pp. 22–28.
- [30] R. A. Farrugia, C. Galea, and C. Guillemot, "Super resolution of light field images using linear subspace projection of patch-volumes," *IEEE Journal of Selected Topics in Signal Processing*, vol. 11, no. 7, pp. 1058–1071, 2017.
- [31] M. Alain and A. Smolic, "Light field super-resolution via lfbm5d sparse coding," in *2018 25th IEEE international conference on image processing (ICIP)*. IEEE, 2018, pp. 2501–2505.
- [32] K. Egiazarian and V. Katkovnik, "Single image super-resolution via bm3d sparse coding," in *2015 23rd European signal processing conference (EUSIPCO)*. IEEE, 2015, pp. 2849–2853.
- [33] M. Rossi and P. Frossard, "Geometry-consistent light field super-resolution via graph-based regularization," *IEEE Transactions on Image Processing*, vol. 27, no. 9, pp. 4207–4218, 2018.
- [34] Y. Yoon, H.-G. Jeon, D. Yoo, J.-Y. Lee, and I. S. Kweon, "Light-field image super-resolution using convolutional neural network," *IEEE Signal Processing Letters*, vol. 24, no. 6, pp. 848–852, 2017.
- [35] S. Wang, T. Zhou, Y. Lu, and H. Di, "Detail preserving transformer for light field image super-resolution," in *AAAI Conference on Artificial Intelligence (AAAI)*, 2022.
- [36] Y. Wang, L. Wang, J. Yang, W. An, J. Yu, and Y. Guo, "Spatial-angular interaction for light field image super-resolution," in *ECCV*, 2020, pp. 290–308.
- [37] S. Zhang, Y. Lin, and H. Sheng, "Residual networks for light field image super-resolution," in *Proceedings of the IEEE/CVF Conference on Computer Vision and Pattern Recognition*, 2019, pp. 11 046–11 055.
- [38] H. Zhang, M. Cisse, Y. N. Dauphin, and D. Lopez-Paz, "mixup: Beyond empirical risk minimization," *arXiv preprint arXiv:1710.09412*, 2017.
- [39] T. DeVries and G. W. Taylor, "Improved regularization of convolutional neural networks with cutout," *arXiv preprint arXiv:1708.04552*, 2017.
- [40] S. Yun, D. Han, S. J. Oh, S. Chun, J. Choe, and Y. Yoo, "Cutmix: Regularization strategy to train strong classifiers with localizable features," in *Proceedings of the IEEE/CVF international conference on computer vision*, 2019, pp. 6023–6032.
- [41] K. Kumar Singh and Y. Jae Lee, "Hide-and-seek: Forcing a network to be meticulous for weakly-supervised object and action localization," in *Proceedings of the IEEE International Conference on Computer Vision*, 2017, pp. 3524–3533.
- [42] E. D. Cubuk, B. Zoph, D. Mane, V. Vasudevan, and Q. V. Le, "Autoaugment: Learning augmentation policies from data," *arXiv preprint arXiv:1805.09501*, 2018.
- [43] H. Bao, L. Dong, S. Piao, and F. Wei, "Beit: Bert pre-training of image transformers," *arXiv preprint arXiv:2106.08254*, 2021.
- [44] K. He, X. Chen, S. Xie, Y. Li, P. Dollár, and R. Girshick, "Masked autoencoders are scalable vision learners," in *Proceedings of the IEEE/CVF conference on computer vision and pattern recognition*, 2022, pp. 16 000–16 009.
- [45] V. Verma, A. Lamb, C. Beckham, A. Najafi, I. Mitliagkas, D. Lopez-Paz, and Y. Bengio, "Manifold mixup: Better representations by interpolating hidden states," in *International conference on machine learning*. PMLR, 2019, pp. 6438–6447.

- [46] X. Gastaldi, “Shake-shake regularization,” *arXiv preprint arXiv:1705.07485*, 2017.
- [47] Y. Yamada, M. Iwamura, T. Akiba, and K. Kise, “Shakedrop regularization for deep residual learning,” *IEEE Access*, vol. 7, pp. 186 126–186 136, 2019.
- [48] G. Larsson, M. Maire, and G. Shakhnarovich, “Fractalnet: Ultra-deep neural networks without residuals,” *arXiv preprint arXiv:1605.07648*, 2016.
- [49] R. Timofte, R. Rothe, and L. Van Gool, “Seven ways to improve example-based single image super resolution,” in *Proceedings of the IEEE conference on computer vision and pattern recognition*, 2016, pp. 1865–1873.
- [50] R. Feng, J. Gu, Y. Qiao, and C. Dong, “Suppressing model overfitting for image super-resolution networks,” in *Proceedings of the IEEE/CVF Conference on Computer Vision and Pattern Recognition Workshops*, 2019, pp. 0–0.
- [51] M. Levoy and P. Hanrahan, “Light field rendering,” in *Proceedings of the 23rd annual conference on Computer graphics and interactive techniques*, 1996, pp. 31–42.
- [52] N. Srivastava, G. Hinton, A. Krizhevsky, I. Sutskever, and R. Salakhutdinov, “Dropout: a simple way to prevent neural networks from overfitting,” *The journal of machine learning research*, vol. 15, no. 1, pp. 1929–1958, 2014.
- [53] C. Shin, H.-G. Jeon, Y. Yoon, I. S. Kweon, and S. J. Kim, “Epinet: A fully-convolutional neural network using epipolar geometry for depth from light field images,” in *Proceedings of the IEEE/CVF Conference on Computer Vision and Pattern Recognition*, 2018, pp. 4748–4757.
- [54] Z. Huang, X. Hu, Z. Xue, W. Xu, and T. Yue, “Fast light-field disparity estimation with multi-disparity-scale cost aggregation,” in *IEEE International Conference on Computer Vision (ICCV)*, 2021, pp. 6320–6329.
- [55] M. Rerabek and T. Ebrahimi, “New light field image dataset,” in *8th International Conference on Quality of Multimedia Experience (QoMEX)*, 2016.
- [56] K. Honauer, O. Johannsen, D. Kondermann, and B. Goldluecke, “A dataset and evaluation methodology for depth estimation on 4d light fields,” in *Asian conference on computer vision (ACCV)*. Springer, 2016, pp. 19–34.
- [57] M. Le Pendu, X. Jiang, and C. Guillemot, “Light field inpainting propagation via low rank matrix completion,” *IEEE Transactions on Image Processing*, vol. 27, no. 4, pp. 1981–1993, 2018.
- [58] V. Vaish and A. Adams, “The (new) stanford light field archive,” *Computer Graphics Laboratory, Stanford University*, vol. 6, no. 7, p. 3, 2008.
- [59] Z. Wang, A. C. Bovik, H. R. Sheikh, and E. P. Simoncelli, “Image quality assessment: from error visibility to structural similarity,” *IEEE transactions on image processing*, vol. 13, no. 4, pp. 600–612, 2004.
- [60] S. Zhang, H. Sheng, C. Li, J. Zhang, and Z. Xiong, “Robust depth estimation for light field via spinning parallelogram operator,” *Computer Vision and Image Understanding*, vol. 145, pp. 148–159, 2016.
- [61] A. S. Raj, M. Lowney, and R. Shah, “Stanford lytro light field archive,” <http://lightfields.stanford.edu/LF2016.html>, 2016.
- [62] J. Chen, J. Hou, and L.-P. Chau, “Light field denoising via anisotropic parallax analysis in a cnn framework,” *IEEE Signal Processing Letters*, vol. 25, no. 9, pp. 1403–1407, 2018.
- [63] M. Guo, J. Hou, J. Jin, J. Chen, and L.-P. Chau, “Deep spatial-angular regularization for light field imaging, denoising, and super-resolution,” *IEEE Transactions on Pattern Analysis and Machine Intelligence*, vol. 44, no. 10, pp. 6094–6110, 2021.
- [64] S. Park, S. Yu, B. Moon, S. Ko, and J. Paik, “Low-light image enhancement using variational optimization-based retinex model,” *IEEE Transactions on Consumer Electronics*, vol. 63, no. 2, pp. 178–184, 2017.
- [65] K. G. Lore, A. Akintayo, and S. Sarkar, “Llnet: A deep autoencoder approach to natural low-light image enhancement,” *Pattern Recognition*, vol. 61, pp. 650–662, 2017.
- [66] S. Zhang, N. Meng, and E. Y. Lam, “Lrt: an efficient low-light restoration transformer for dark light field images,” *IEEE Transactions on Image Processing*, 2023.
- [67] C. Liu and D. Sun, “On bayesian adaptive video super resolution,” *IEEE transactions on pattern analysis and machine intelligence*, vol. 36, no. 2, pp. 346–360, 2013.
- [68] S. Bell-Kligler, A. Shocher, and M. Irani, “Blind super-resolution kernel estimation using an internal-gan,” *Advances in Neural Information Processing Systems*, vol. 32, 2019.
- [69] K. Zhang, L. V. Gool, and R. Timofte, “Deep unfolding network for image super-resolution,” in *Proceedings of the IEEE/CVF conference on computer vision and pattern recognition*, 2020, pp. 3217–3226.
- [70] J. Gu, H. Lu, W. Zuo, and C. Dong, “Blind super-resolution with iterative kernel correction,” in *Proceedings of the IEEE/CVF Conference on Computer Vision and Pattern Recognition*, 2019, pp. 1604–1613.
- [71] Y. Huang, S. Li, L. Wang, T. Tan *et al.*, “Unfolding the alternating optimization for blind super resolution,” *Advances in Neural Information Processing Systems*, vol. 33, pp. 5632–5643, 2020.